Continental Shelf Research 143 (2017) 219–227

Contents lists available at ScienceDirect

Continental Shelf Research

journal homepage: www.elsevier.com/locate/csr

Research papers

Coastal tomographic mapping of nonlinear tidal currents and residual currents

Ze-Nan Zhu[a,b], Xiao-Hua Zhu[b,a,*], Xinyu Guo[b,c]

[a] Ocean College, Zhejiang University, Zhoushan 316021, China
[b] State Key Laboratory of Satellite Ocean Environment Dynamics, Second Institute of Oceanography, State Oceanic Administration, Hangzhou 310012, China
[c] Center for Marine Environmental Study, Ehime University, 2-5 Bunkyo-cho, Matsuyama 790-8577, Japan

ARTICLE INFO

Keywords:
Nonlinear tidal currents
Residual currents
M_4 and M_6 generation mechanisms
Coastal acoustic tomography

ABSTRACT

Depth-averaged current data, which were obtained by coastal acoustic tomography (CAT) July 12–13, 2009 in Zhitouyang Bay on the western side of the East China Sea, are used to estimate the semidiurnal tidal current (M_2) as well as its first two overtide currents (M_4 and M_6). Spatial mean amplitude ratios M_2:M_4:M_6 in the bay are 1.00:0.15:0.11. The shallow-water equations are used to analyze the generation mechanisms of M_4 and M_6. In the deep area, where water depths are larger than 60 m, M_4 velocity amplitudes measured by CAT agree well with those predicted by the advection terms in the shallow water equations, indicating that M_4 in the deep area is predominantly generated by the advection terms. M_6 measured by CAT and M_6 predicted by the nonlinear quadratic bottom friction terms agree well in the area where water depths are less than 20 m, indicating that friction mechanisms are predominant for generating M_6 in the shallow area. In addition, dynamic analysis of the residual currents using the tidally averaged momentum equation shows that spatial mean values of the horizontal pressure gradient due to residual sea level and of the advection of residual currents together contribute about 75% of the spatial mean values of the advection by the tidal currents, indicating that residual currents in this bay are induced mainly by the nonlinear effects of tidal currents. This is the first ever nonlinear tidal current study by CAT.

1. Introduction

The overtides M_4 and M_6, are common shallow-water constituents in coastal regions where the M_2 tide is dominant. They are generated when the tide propagates into a shallow-water area. Sea level observational data (e.g., Aubrey and Speer (1985), Speer and Aubrey (1985)) have shown obvious distortion from the combination of the M_2 tide with its overtides. But there are few observational data of M_4 and M_6 overtides in tidal current data over a large area.

Sea level observations (Aubrey and Speer, 1985; Parker, 1991) and tidal current observations (Blanton et al., 2002; Parker, 1991) have shown that presence of the M_4 tide is a general feature of many estuaries or coastal regions. Then theoretical analyses (Speer and Aubrey, 1985; Friedrichs and Aubrey, 1988; Parker, 1991) and numerical models (Pingree and Maddock, 1978; Hench and Luettich, 2003; Sheng and Wang, 2004) have indicated that the continuity and advection terms are the main contributors to generation of the M_4 tide. Sheng and Wang (2004) demonstrated that the advection terms are most important for generating the M_4 tide in Lunenburg Bay, Nova Scotia, while Pingree and Maddock (1978) pointed out that continuity terms played a more important role in the English Channel. Therefore the M_4 generation mechanisms are complicated and can be different in different regions.

Earlier studies of the M_6 tide are mainly based on theoretical derivation, with Fourier expansion of quadratic bottom friction (Fang, 1987; Parker, 1991; Le Provost, 1991). They point out that quadratic bottom friction is partly nonlinear, and the nonlinear part plays an important role in generating the M_6 tide. Observational data (Blanton et al., 2002) and numerical models (Sheng and Wang, 2004) have also been used to discuss the M_6 tide generation mechanisms, and confirm that quadratic bottom friction plays an important role in generating the M_6 tide.

Previous M_4 and M_6 tide analyses based on observational data mainly used sea level data rather than tidal current data (e.g., Aubrey and Speer (1985), Parker (1991), Dong and Su (1991a)). Idealized experiments (e.g., Pingree and Maddock (1980) and Hench et al.

* Corresponding author at: State Key Laboratory of Satellite Ocean Environment Dynamics, Second Institute of Oceanography, State Oceanic Administration, Hangzhou 310012, China.
E-mail address: xhzhu@sio.org.cn (X.-H. Zhu).

http://dx.doi.org/10.1016/j.csr.2016.06.014
Received 16 November 2015; Received in revised form 12 June 2016; Accepted 24 June 2016
Available online 25 June 2016

(2002)) and numerical models (e.g., Dong and Su (1991b), Walters and Werner (1991)) were widely used to understand the dynamics of nonlinear tides. The dynamical mechanisms of nonlinear tides have been well documented by these studies.

In previous studies, the observational current data were mainly point measurements from current meters (e.g., Blanton et al. (2002) and Parker (1991)), which do not readily enable mapping of the tidal current structure over a large area. In order to examine M_4 generation mechanisms, the 2-dimensional continuous current field should be mapped accurately to allow calculation of the advection terms. However, with conventional measurement techniques it is difficult to deploy a large number of current meters within an observation region to obtain the needed 2-dimensional continuous current field. Coastal Acoustic Tomography (CAT) can achieve this easily by deploying only a few instruments on the periphery of the observation region (Yamaoka et al., 2002). Thus, we can analyze the generation mechanisms of M_4 and M_6 using the current field mapped with the CAT.

In order to study the dynamics of overtides M_4 and M_6 using CAT data, we chose for our research region a shallow bay, Zhitouyang Bay (hereinafter ZTYB) having a mean water depth of about 25 m and complex topography, which is beneficial for generating nonlinear tides. Zhu et al. (2013) had already determined the horizontal distribution of tidal currents and residual currents in ZTYB by using CAT (Fig. 1). They pointed out that the M_2 tide was the predominant tidal constituent, and the M_2 velocity amplitudes reached 1.0 m s^{-1}. The residual currents were largest along the deep channel, with a spatial mean speed of 0.2 m s^{-1}. Thus, relatively large overtides of the M_2 tide were expected. But they did not further discuss the M_2 overtides and the dynamics of the residual current. The correlation coefficient between the M_2 tidal current amplitude and the residual current speed is 0.52 (Fig. 2), indicating that the residual current may be induced by the tidal currents. Moreover, these data of Zhu et al. (2013) are ideal for analyzing the M_2 overtides and the relative importance of different generation mechanisms of these overtides.

In this paper, we use the CAT data to estimate the M_4 and M_6 tidal current ellipses. Then we calculate the M_4 tidal current ellipses obtained from the nonlinear advection terms in the shallow water equations (hereinafter, M_{4_cal}) and the M_6 tidal current ellipses obtained from the nonlinear components of the quadratic bottom friction terms (hereinafter, M_{6_cal}) to demonstrate the M_4 and M_6 overtide generation mechanisms. We also discuss the residual current dynamical mechanisms in the observation region by using the tidally averaged momentum equation.

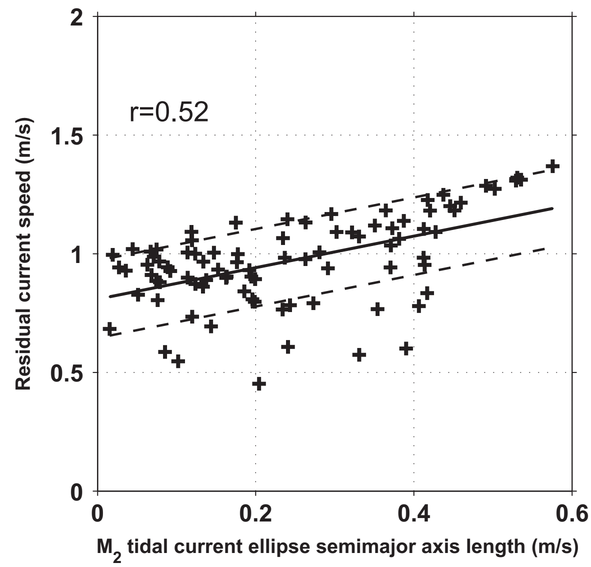

Fig. 2. Correlation between M_2 tidal current amplitude and residual current speed. The thin solid line indicates the regression line derived from the least-squares method. The two gray broken lines indicate the standard deviation range.

2. Data set

The data used in this study were obtained from the CAT observation experiment in ZTYB (Fig. 1). The 3-min interval travel-time difference raw data were measured for about 27 h during July 12–13, 2009 (Zhu et al., 2013). With 27 h observation, we can extract information of semidiurnal tides as represented by M_2 tidal constituent and of diurnal tides as represented by K_1 tidal constituent as well as that of overtides of M_4 and M_6 tidal constituents.

In order to obtain the horizontal distribution of the depth averaged current field from the differential travel-time data measured by CAT, the inverse method (Park and Kaneko, 2001) was used. The equation for the inverse method is as follows:

$$\boldsymbol{y} = \boldsymbol{E}\boldsymbol{x} + \boldsymbol{e}, \tag{1}$$

where $\boldsymbol{y}$ is a 21-element column vector, each column denotes the travel-time difference data of each station pair; $\boldsymbol{x}$ is a vector of the 20-element row vector of the unknown coefficients used in the Fourier function expansion of the stream function used to estimate the current field; $\boldsymbol{E}$ is a 21×20 matrix, determined by the locations of the 7 CAT stations; $\boldsymbol{e}$ is the error vector. The optimum solution of Eq. (1) is obtained by minimizing the objective function ($\boldsymbol{J}$) with the tapered

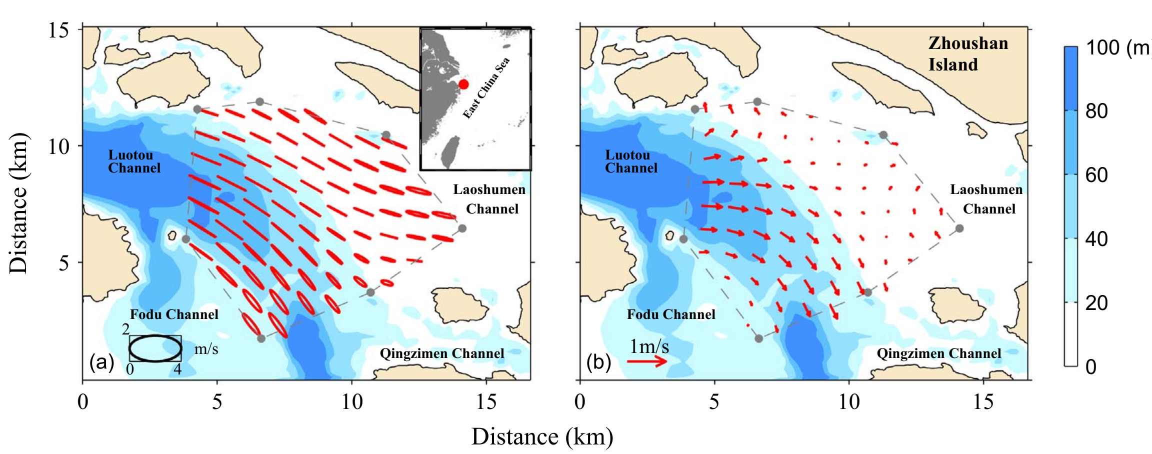

Fig. 1. The distribution of (a) M_2 tidal current ellipses, and (b) residual currents in Zhitouyang Bay, observed by Zhu et al. (2013). The gray solid circles are the positions of the CAT stations (C1–C7). The area enclosed by the dashed lines indicates the CAT observational region. The figure in the upper right of panel (a) shows the East China Sea with a red circle denoting the location of the study. (For interpretation of the references to color in this figure legend, the reader is referred to the web version of this article).

least squares method. The objective function is given by:

$$\boldsymbol{J} = (\boldsymbol{y} - \boldsymbol{E}\boldsymbol{x})^T(\boldsymbol{y} - \boldsymbol{E}\boldsymbol{x}) + \alpha^2\boldsymbol{x}^T\boldsymbol{x}, \tag{2}$$

where the weighting factor α is determined by the L-curve method (Hansen and O'Leary, 1993).

Grid size for the data display in the inverse analysis is set to be 1.0×1.0 km, which is the same as that used in Zhu et al. (2013).

For a traditional harmonic tidal theory (Godin, 1972), an observed current velocity time series $v(t)$ can be written in the following form:

$$v(t) = v_0(t) + \sum_{i=1}^{m}(A_i\sin\sigma_i t + B_i\cos\sigma_i t) \tag{3}$$

where i denotes tidal constituents, A_i, B_i are harmonic constants, σ_i is the angular frequency, t denotes the time, $v_0(t)$ is the residual current. Following this style, the tidal currents of M_4 and M_6 can be written as:

$$\begin{cases} v_{M_4}(t) = A_{M_4}\sin\sigma_{M_4}t + B_{M_4}\cos\sigma_{M_4}t \\ v_{M_6}(t) = A_{M_6}\sin\sigma_{M_6}t + B_{M_6}\cos\sigma_{M_6}t \end{cases} \tag{4}$$

where, A_{M_4}, B_{M_4}, A_{M_6}, B_{M_6} are harmonic constants of M_4 and M_6, respectively. σ_{M_4}, σ_{M_6} (i.e., 1.01 and 1.52 h^{-1}) are the angular frequencies of M_4 and M_6. After obtaining the current field at each spatial grid point for a period of 27 h by using the inverse method, we then compute the M_4 and M_6 harmonic constants at each grid point by using harmonic tidal analysis (Pawlowicz et al., 2002).

The minimum observation time for separating the M_4 and M_6 is $\frac{2\pi}{\sigma_{M_6} - \sigma_{M_4}}$=12.4 h, when the time interval of data is one hour (Godin, 1972). Our data length is about 27 h which is longer than 12.4 h and is sufficient to separate the M_4 and M_6 constituents. On the other hand, to resolve well the M_4 and M_6 overtides, we used 15-min running means of CAT data, instead of the hourly running means used in Zhu et al. (2013). This 15-minute time interval in our data allows us to have at least 16 data points in the M_6 period and more than that in the M_4 period. The root mean square differences (RMSDs) of the differential travel-time data between the 15-minute running mean data and the hourly running mean data range from 0.05 to 0.30 ms, and the corresponding RMSDs of velocity range from 0.01 to 0.06 m s^{-1}. Thus, the 15-min running mean data are credible in this study.

3. Theoretical derivation of M_4 and M_6

After the tide propagates into a shallow-water region, the nonlinear terms in the momentum equations become non-negligible; the nonlinear advection term and the nonlinear friction term are the important terms in the momentum equations (Fang, 1987). To obtain the M_4 and M_6 tidal currents generated by the advection and quadratic bottom friction terms, the derivation of these terms in the two-dimensional shallow-water equations has been done. In our theoretical derivation, the two-dimensional shallow-water equations (Le Provost, 1991) can be written as follows:

$$\begin{cases} \frac{\partial u}{\partial t} + u\frac{\partial u}{\partial x} + v\frac{\partial u}{\partial y} - fv = -g\frac{\partial \eta}{\partial x} - \frac{C_d}{h+\eta}u\sqrt{u^2+v^2} \\ \frac{\partial v}{\partial t} + u\frac{\partial v}{\partial x} + v\frac{\partial v}{\partial y} + fu = -g\frac{\partial \eta}{\partial y} - \frac{C_d}{h+\eta}v\sqrt{u^2+v^2} \end{cases} \tag{5}$$

Here, x, y are the horizontal spatial coordinates (positive denoting eastward and northward respectively), t is time, u, v are the horizontal velocity components; g is gravitational acceleration (=9.8 m s^{-2}); η is surface elevation; C_d is bottom drag coefficient (=0.0025); h is the water depth; f is Coriolis parameter (=7.27×10^{-5} s^{-1}). Thus, the nonlinear advection terms are $u\frac{\partial u}{\partial x}+v\frac{\partial u}{\partial y}$ and $u\frac{\partial v}{\partial x}+v\frac{\partial v}{\partial y}$; the nonlinear friction terms are $\frac{C_d}{h+\eta}u\sqrt{u^2+v^2}$ and $\frac{C_d}{h+\eta}v\sqrt{u^2+v^2}$. We then derive the two-dimensional shallow-water equations in the following steps.

The tidal velocity components of M_2 (i.e., u_σ and v_σ) can be written as

$$\begin{cases} u_\sigma = U_c(x, y)\cos(\sigma t) + U_s(x, y)\sin(\sigma t) \\ v_\sigma = V_c(x, y)\cos(\sigma t) + V_s(x, y)\sin(\sigma t) \end{cases} \tag{6}$$

Here, $U_c(x, y)$, $U_s(x, y)$, $V_c(x, y)$, $V_s(x, y)$ are harmonic constants of the M_2 tidal current at each spatial point, σ is the M_2 angular frequency.

The M_4 tide is mainly caused by the nonlinear advection terms of the M_2 tidal current (Parker, 1991). Substituting Eq. (6) into Eq. (5), we find that the nonlinear advection terms can be written as follows:

$$\begin{cases} A_0 + B_c\cos(2\sigma t) + B_s\sin(2\sigma t) \\ C_0 + D_c\cos(2\sigma t) + D_s\sin(2\sigma t) \end{cases} \tag{7}$$

Here,

$$A_0 = \frac{1}{2}\left(U_c\frac{\partial U_c}{\partial x} + V_c\frac{\partial U_c}{\partial y} + U_s\frac{\partial U_s}{\partial x} + V_s\frac{\partial U_s}{\partial y}\right); C_0 = \frac{1}{2}\left(U_c\frac{\partial V_c}{\partial x} + V_c\frac{\partial V_c}{\partial y} + U_s\frac{\partial V_s}{\partial x} + V_s\frac{\partial V_s}{\partial y}\right);$$

$$B_c = \frac{1}{2}\left(U_c\frac{\partial U_c}{\partial x} + V_c\frac{\partial U_c}{\partial y} + U_s\frac{\partial U_s}{\partial x} + V_s\frac{\partial U_s}{\partial y}\right); B_s = \frac{1}{2}\left(U_c\frac{\partial U_s}{\partial x} + U_s\frac{\partial U_c}{\partial x} + V_c\frac{d U_s}{\partial y} + V_s\frac{\partial U_c}{\partial y}\right);$$

$$D_c = \frac{1}{2}\left(U_c\frac{\partial V_c}{\partial x} + V_c\frac{\partial V_c}{\partial y} + U_s\frac{\partial V_s}{\partial x} + V_s\frac{\partial V_s}{\partial y}\right); D_s = \frac{1}{2}\left(U_c\frac{\partial V_s}{\partial x} + U_s\frac{\partial V_c}{\partial x} + V_c\frac{\partial V_s}{\partial y} + V_s\frac{\partial V_c}{\partial y}\right).$$

Then we can obtain the currents from the advection terms (i.e., M_{4_cal}) by integrating the M_4 angular frequency terms in Eq. (7) with respect to time, as follows:

$$\begin{cases} u_{2\sigma} = \frac{B_0}{2\sigma}\sin(2\sigma t - \alpha_u) \\ v_{2\sigma} = \frac{D_0}{2\sigma}\sin(2\sigma t - \alpha_v) \end{cases} \tag{8}$$

Here, $B_0 = \sqrt{B_c^2 + B_s^2}$; $D_0 = \sqrt{D_c^2 + D_s^2}$; $\alpha_u = \arctan\left(\frac{B_s}{B_c}\right)$; $\alpha_v = \arctan\left(\frac{D_s}{D_c}\right)$. The velocities in Eq. (8), having the M_4 angular frequency, are considered to be the predicted M_4 tidal currents. Then, because the predicted M_4 currents are derived from the advection terms, if the predicted M_4 are similar to the M_4 currents measured by CAT, we can confirm that the advection terms make a primary contribution to the generation of M_4 tidal currents, otherwise the M_4 tidal currents may also be generated by other factors or propagate to the observation site from adjacent regions.

On the other hand, the overtide that has three times the M_2 angular frequency (i.e., 3σ) is mainly caused by the friction terms (Fang, 1987; Parker, 1991; Le Provost, 1991). The quadratic bottom friction terms of the linear tide can be written in the following form:

$$\begin{cases} \tau_{\text{maj}} = C_d\left|\sqrt{u_{\text{maj}}^2 + u_{\text{min}}^2}\right|u_{\text{maj}}/h \\ \tau_{\text{min}} = C_d\left|\sqrt{u_{\text{maj}}^2 + u_{\text{min}}^2}\right|u_{\text{min}}/h \end{cases} \tag{9}$$

Here, τ_{maj} and τ_{min} are the bottom friction along the major and minor axis directions of the linear tide, respectively; u_{maj} and u_{min} are the velocities along the major and minor axis directions of the linear tide, respectively; h is the water depth. Considering $u_{maj} \gg u_{min}$ (Fig. 1), Eq. (9) can be written as

$$\begin{cases} \tau_{\text{maj}} = C_d|u_{\text{maj}}|u_{\text{maj}}/h \\ \tau_{\text{min}} = C_d|u_{\text{maj}}|u_{\text{min}}/h \end{cases} \tag{10}$$

Eq. (6) can also be written in the following form:

$$\begin{cases} u_{\mathrm{maj}} = U_{\mathrm{maj}}(x,\ y)\cos\sigma t \\ u_{\mathrm{min}} = U_{\mathrm{min}}(x,\ y)\sin\sigma t \end{cases} \tag{11}$$

Here, U_{maj} and U_{min} are the amplitudes along the major and minor axis directions of the linear tide, respectively.

When we consider only one linear tidal constituent, the Fourier expansion of Eq. (10) can be written as follows:

$$\begin{cases} \tau_{\mathrm{maj}} = U_{\mathrm{maj}}(x,\ y)^2 \sum_{m=0,1,2,3,\ldots} (-1)^{m+1} \frac{8}{(2m-1)(2m+1)(2m+3)\pi} \cos(2m+1)\sigma t \\ \tau_{\mathrm{min}} = U_{\mathrm{maj}}\left(x,\ y\right) U_{\mathrm{min}}\left(x,\ y\right) \sum_{m=0,1,2,3,\ldots} (-1)^{m} \frac{8}{(2m-1)(2m+3)\pi} \sin(2m+1)\sigma t \end{cases} \tag{12}$$

The predicted M_6 tidal currents (i.e., M_{6_cal}) are obtained by setting m=1 and integrating Eq. (12) with respect to time as follows:

$$\begin{cases} u_{3\sigma} = U_{\mathrm{maj}}(x,\ y)^2 \frac{8C_d}{45h\pi} \cos 3\sigma t \\ v_{3\sigma} = -U_{\mathrm{maj}}(x,\ y) U_{\mathrm{min}}(x,\ y) \frac{4C_d}{15h\pi} \sin 3\sigma t \end{cases} \tag{13}$$

The velocities in Eq. (13) having the M_6 angular frequency are considered to be the predicted M_6 tide. From the similarity between the measured M_6 and predicted M_6 currents, we can confirm the contribution of quadratic bottom friction to the generation of the M_6 tide. Here we should note that the phases in Eq. (11) are ignored to make derivation of the Fourier expansion easier.

In this theoretical derivation, we firstly substitute the tidal current forms of M_2 (Eqs. (6) and (11)) into the advection terms and quadratic bottom friction terms of the shallow water equations (Eq. (5)), respectively. Then, we obtain the terms having the M_4 and M_6 frequencies (Eqs. (8) and (13)) as the predicted M_4 and M_6 tidal currents. Comparing the predicted M_4 and M_6 currents (i.e., Eqs. (8) and (13)) with those observed directly by CAT, we can quantify the contribution of advection terms and quadratic bottom friction terms for generating M_4 and M_6.

4. Results and discussion

We estimate the tidal constituents and their errors by a tidal harmonic analysis using the T_TIDE program (Pawlowicz et al., 2002). For tidal currents in ZTYB, M_2 is the strongest constituent. The M_2 tidal current ellipses calculated using the 15-min running mean data have no significant differences from the hourly running mean results of Zhu et al. (2013) (Fig. 1). The spatial mean semimajor and semiminor axis lengths of the M_2 tidal ellipses are 0.97 and 0.07 m s^{-1}, respectively. We estimate the spatial mean errors of M_2, M_4 and M_6 velocity amplitudes as 0.06 m s^{-1}, 0.05 m s^{-1} and 0.05 m s^{-1}, respectively. Here we should note that, due to the duration of the observation data, we use M_2 as representative of the semidiurnal tidal constituents.

4.1. Results for M_4 tidal currents

The horizontal distribution of the M_4 tidal ellipses measured by CAT and those of M_{4_cal} are shown in Fig. 3. The M_4 currents (Fig. 3a) are relatively large near the Luotou and Qinzimen channels with a maximum value 0.27 m s^{-1}, corresponding well to the distribution of the M_2 tidal current (Fig. 1). The area averaged semimajor and semiminor axis lengths of the M_4 tidal ellipses are 0.15 and 0.04 m s^{-1}, respectively (Table 1). The spatial mean ellipticity of the M_4 tide is 0.27, which is larger than that of M_2 (0.07). The M_{4_cal} currents (Fig. 3b) are also relatively larger near the Luotou and Qinzimen channels with a maximum value 0.32 m s^{-1} near Luotou channel. The M_{4_cal} ellipses have the same area averaged semimajor and semiminor axis lengths as the observed M_4 values (Table 1).

The M_4 semimajor axis direction is mainly northeast-southwest in the west part of the observation region, and becomes northwest-southeast in the east part (Fig. 3a). The M_{4_cal} semimajor axis direction is mainly northeast-southwest in the west part of the region, and becomes north-south in the east part (Fig. 3b).

Comparing the results for the tidal ellipses of M_4 (Fig. 3a) and M_{4_cal} (Fig. 3b), the spatial distributions agree better in the west part of the observational region (red ellipses in Fig. 3) where the directions of the semimajor axes of both sets of ellipses are mainly northeast-southwest. The area averaged semimajor and semiminor axis lengths are the same for the two sets. The difference between their maximum speeds (0.27 m s^{-1} and 0.32 m s^{-1}, respectively) is 0.05 m s^{-1}, which is less than the standard deviation (STD) of the amplitude differences between M_4 and M_{4_cal} (0.07 m s^{-1}). From such close maximum speeds of M_4 and M_{4_cal}, we therefore confirm that the advection terms play an important role in generating M_4 currents in ZTYB.

Furthermore, we compare the velocity amplitudes of M_4 and M_{4_cal} to confirm the contribution of advection terms in generating the M_4 tide in different areas of the observational region. The relationship between the M_4 and M_{4_cal} velocity amplitudes and phase is shown in Fig. 4. In this figure we see that not all the data are gathered around the "perfect agreement" diagonal line. We consider the M_4 and M_{4_cal} ellipses to be similar at those points (red dots in Fig. 4) for which the differences of both velocity amplitude and phase between M_4 and M_{4_cal} are less than one STD of the differences between the M_4 and M_{4_cal} values, i.e., 0.07 m s^{-1} and 110°, respectively. The corresponding ellipses are shown in red in Fig. 3; we find that the tidal current ellipses are most similar in the deep area where water depths are larger than 60 m. The distribution of M_2 ellipses (Fig. 1a) shows that

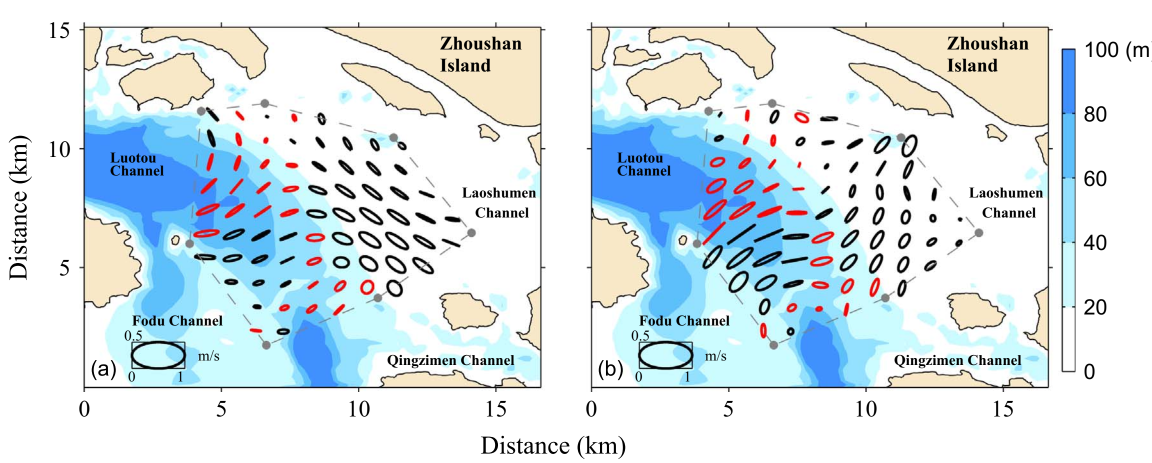

Fig. 3. Tidal current ellipses of (a) M_4, and (b) M_{4_cal}. Red lines indicate similar ellipses for M_4 and M_{4_cal}. The area enclosed by the dashed lines indicates the CAT observational region. (For interpretation of the references to color in this figure legend, the reader is referred to the web version of this article.)

Table 1
Spatial mean parameters of tidal current ellipses of M_4 and M_{4_cal} and their STDs.

	Semimajor axis length ± STDs (m s^{-1})	Semiminor axis length ± STDs (m s^{-1})
M_4	0.15 ± 0.05	0.04 ± 0.03
M_{4_cal}	0.15 ± 0.07	0.04 ± 0.03

relatively large M_2 currents appear in the deep area, which means the values of the advection terms are also larger in the deep area. Thus the advection terms make a primary contribution to M_4 generation in the deep area. Moreover the tidal current ellipses (black ellipses in Fig. 3) are not generally similar in shallow waters, that is to say the M_4 tidal currents in the shallow area are not mainly caused by the advection terms. There are other key factors for generating M_4 in the shallow area, such as the continuity terms or the friction mechanism (Parker, 1991).

4.2. Results of M_6 tidal currents

The horizontal distribution of the M_6 tidal ellipses measured by CAT and those of M_{6_cal} are shown in Fig. 5. The maximum value of the M_6 semimajor axes is 0.20 m s^{-1}, appearing near Luotou channel. The spatial mean semimajor and semiminor axis lengths of the M_6 current ellipses are 0.11 and 0.03 m s^{-1} (Table 2). The M_6 ellipticity is relatively small in the north part of the observational region, and becomes larger near Fodu channel. The spatial mean value of ellipticity is 0.27. The M_{6_cal} currents (Fig. 5b) are relatively larger near Luotou channel with a maximum value 0.10 m s^{-1}. The spatial mean semimajor and semiminor axis lengths of the M_{6_cal} tidal current ellipses are 0.07 and 0.01 m s^{-1}, respectively (Table 2). The spatial mean ellipticity of the M_{6_cal} tide is 0.09.

The orientations of the M_6 and M_{6_cal} tidal current ellipses correspond well throughout the observational region: both are mainly directed east-west in the north part of the observational region, and turn north-south along the 40 m bathymetric contour.

Comparing the tidal current ellipses of M_6 (Fig. 5a) and M_{6_cal} (Fig. 5b), we see that the patterns agree well; the directions of the major axes of them both turn north-south along the deep area in the middle of the observational region. The M_6 and M_{6_cal} currents are both relatively large near Luotou channel, and become small near Qinzimen channel, but the M_{6_cal} currents are slightly smaller than those of M_6. These results confirm that the quadratic bottom friction terms play an important role in generating M_6 currents in ZTYB.

We further show the relationship of M_6 and M_{6_cal} velocity amplitudes (Fig. 6) to confirm the contribution of the quadratic bottom friction terms to the generation of M_6 in different areas of the observational region. We consider the M_6 and M_{6_cal} ellipses to be similar at those points (red dots in Fig. 6) for which the difference of velocity amplitude between M_6 and M_{6_cal} is less than the STD of the differences between the M_6 and M_{6_cal} values (i.e., 0.05 m s^{-1}). Where the tidal current ellipses are similar (red ellipses in Fig. 5) this similarity indicates M_6 mainly generated by the quadratic bottom friction terms; this occurs principally in the east part of the observational region where water depth is less than 20 m. These results indicate that the quadratic bottom friction terms play a primary role for generating M_6 in shallow waters, while M_6 in the deep area is also affected by such factors such as the other nonlinear terms in the momentum equations (Sheng and Wang, 2004).

4.3. Asymmetric distortion of M_4 and M_6

From the results above, the spatially-averaged amplitude ratios M_2:M_4:M_6 are 1.00:0.15:0.11. The relatively large M_4 and M_6 overtides generate strong asymmetric distortion in ZTYB. In this section, we discuss the characteristics of this asymmetric distortion by using the ZTYB CAT data.

Asymmetric distortion is mainly caused by the interaction of M_2 and M_4 (Aubrey and Speer, 1985; Speer and Aubrey, 1985; Friedrichs and Aubrey, 1988). The ratio of the velocity amplitudes of M_4 to M_2 (hereinafter M_4/M_2) is calculated to show the asymmetric distortion resulting from M_4 currents in the observational region (Fig. 7a). M_4/M_2 ranges from 0.02 to 0.39 in the observational region. It is relatively small (< 0.2) and varies little in the north and near Fodu channel, while it abruptly increases to its highest value (0.39) near Qinzimen channel, indicating that the asymmetry changes dramatically near

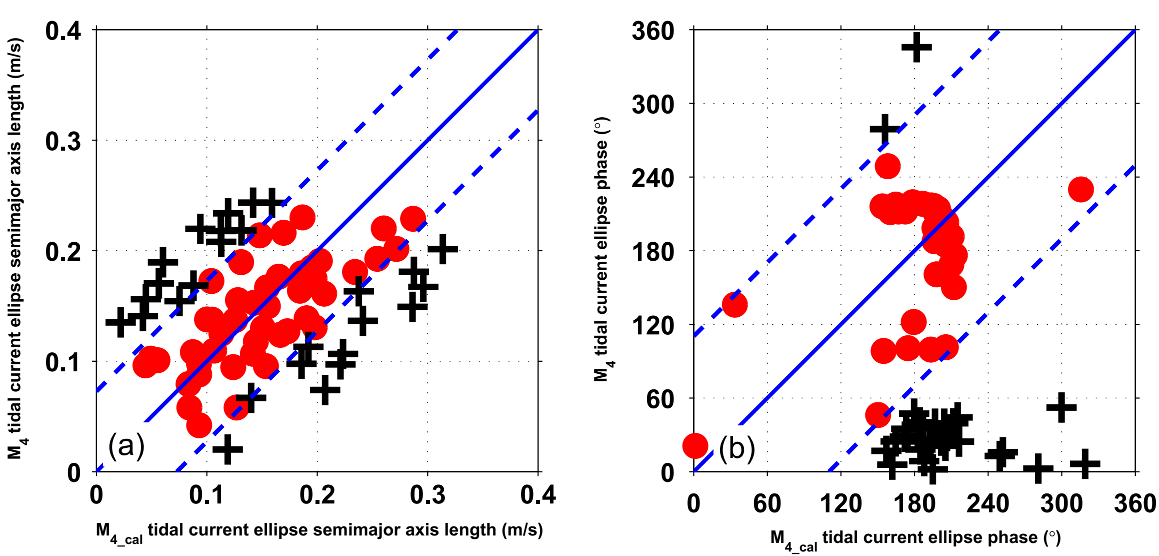

Fig. 4. Scatter plot of M_4 and M_{4_cal} (a) velocity amplitudes, (b) phases. In each panel the diagonal blue solid line denotes perfect agreement, and the blue dashed lines denote the standard deviation (STD) range of the velocity amplitudes from the diagonal line. The red dots (black crosses) indicate points at which the differences of both velocity amplitude and phase between M_4 and M_{4_cal} are less (larger) than the STD of the differences between M_4 and M_{4_cal} (i.e., 0.07 m s^{-1} and 110°). (For interpretation of the references to color in this figure legend, the reader is referred to the web version of this article.)

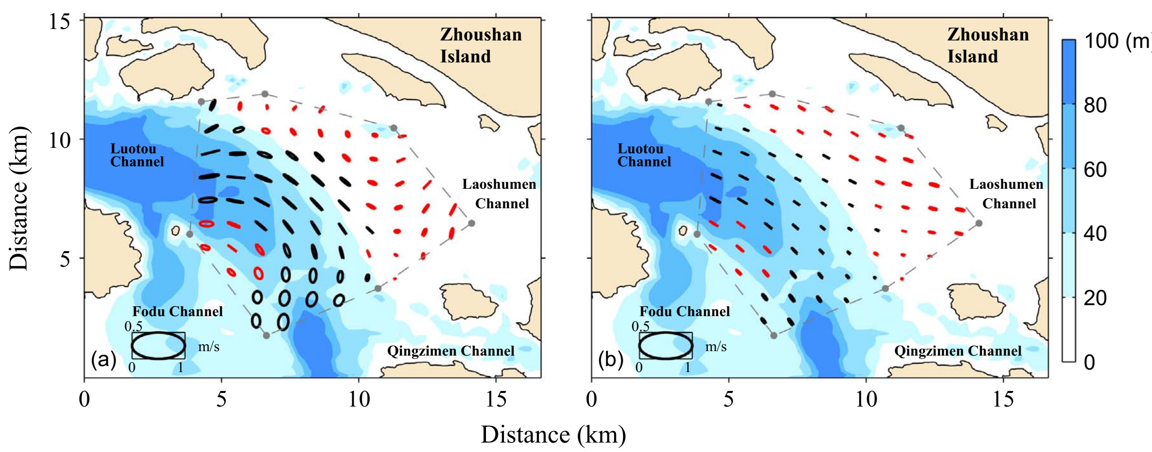

Fig. 5. Tidal current ellipses of (a) M_6, and (b) M_{6_cal}. Red lines indicate similar ellipses for M_6 and M_{6_cal}. The area enclosed by the dashed lines indicates the CAT observational region. (For interpretation of the references to color in this figure legend, the reader is referred to the web version of this article).

Table 2
Spatial mean parameters of tidal current ellipses of M_6 and M_{6_cal} and their STDs.

	Semimajor axis length ± STDs (m s^{-1})	Semiminor axis length ± STDs (m s^{-1})
M_6	0.11 ± 0.04	0.03 ± 0.02
M_{6_cal}	0.07 ± 0.02	0.01 ± 0.00

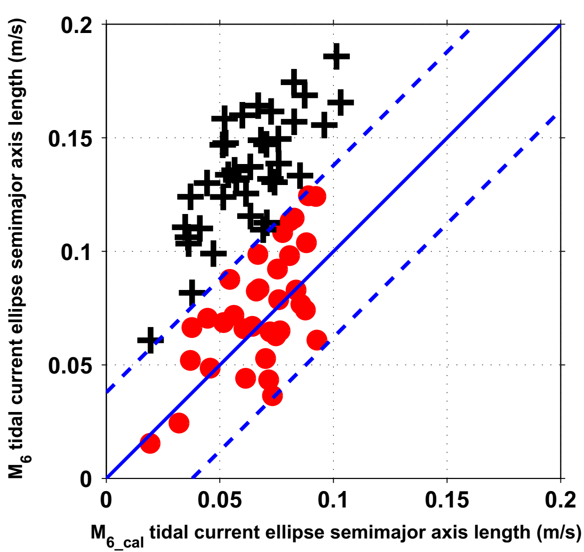

Fig. 6. Scatter plot of M_6 and M_{6_cal} velocity amplitudes. In each panel the diagonal blue solid line denotes perfect agreement, and the blue dashed lines denote the standard deviation (STD) range of the velocity amplitudes from the diagonal line. The red dots (black crosses) indicate the points at which the differences of velocity amplitudes between M_6 and M_{6_cal} are less (larger) than the STD of the differences between M_6 and M_{6_cal} (i.e., 0.05 m s^{-1}). (For interpretation of the references to color in this figure legend, the reader is referred to the web version of this article.)

Qinzimen channel. The type of asymmetric distortion (flood- or ebb-dominant) is determined by the relative phase of $2M_2$-M_4 (Speer and Aubrey, 1985). The relative velocity phase of $2M_2$-M_4 (Fig. 7c) changes gradually from about −90° to 90°, from the west part to the east part of the observational region, indicating that the type of asymmetric distortion is flood-dominant in this area. But the type becomes ebb-dominant ($2M_2$-M_4 relative velocity phase larger than 90°) in the middle area near Qinzimen channel (Friedrichs and Aubrey, 1988). Regardless of type, a larger M_4/M_2 ratio denotes more distortion of the tide (Friedrichs and Aubrey, 1988), so there are relatively strong flood- and ebb-dominant distortions near Qinzimen channel, with weak distortions in the rest of the region. Near Qinzimen channel, the tidal M_4 and M_{4_cal} current ellipses (Fig. 3) are not similar and the M_{4_cal} tidal currents (Fig. 3b) are relatively small, indicating that the advection terms contribute less in this area; furthermore, there are no abrupt changes in M_6/M_2 (Fig. 7b). Thus the continuity terms should be dominant in generating M_4 here, and the M_2 energy should mainly transfer to M_4 (Parker, 1991; Blanton et al., 2002).

M_6 also plays a minor role in the tidal asymmetry (Blanton et al., 2002). The ratio of the velocity amplitudes of M_6 to M_2 (hereinafter M_6/M_2) is also calculated to show the asymmetric distortion resulting from M_6 in the observational region (Fig. 7b). M_6/M_2 is less than 0.2 and changes gradually throughout the observational region. It is relatively small near Fodu channel and in the north part of the region, as in the case of M_4/M_2, while M_6/M_2 is only about 0.05 near Qinzimen channel. Highest M_6/M_2 is observed in middle of the CAT region with a value of 0.17. The relative velocity phase of 3 M_2-M_6 (Fig. 7d) is about 90° in the middle and south part of the observational region. It becomes larger than 90° or less than −90° in the west and east part of the observational region. However, the values of M_6/M_2 (Fig. 7b) are very small (about 0.1), so the asymmetric distortion caused by M_6 is weak (Blanton et al., 2002). Compared with the results of M_4/M_2, M_6/M_2 is relatively small in most of the ZTYB region, indicating that M_6 contributes less to the asymmetric distortion.

4.4. Dynamic mechanisms of residual currents

The depth-averaged residual currents are shown in Fig. 1b. The residual currents are strong at the inflow from Luotou channel and weak in the eastern part of the observation region. The residual current vectors are eastward in the north, then turn southward near Fodu channel. To comprehend the main dynamic processes of the residual currents in ZTYB, we decompose the depth-averaged currents ($\vec{u}=u\vec{i}+v\vec{j}$) observed by CAT into two parts: the tidal currents ($\vec{u}' = u'\vec{i} + v'\vec{j}$) and the residual currents ($\vec{U}=U\vec{i}+V\vec{j}$). The momentum equation, integrated from the sea bottom to the sea surface and averaged over one tidal cycle can be written (Sheng and Wang, 2004; Zhu et al., 2015) as

$$\nabla_h\bullet(\overline{\vec{u}'\vec{u}'})=-g\nabla_h\bar{\eta} - \nabla_h(\vec{U}\vec{U}) + A_m\nabla_h\bullet(\nabla_h\vec{U}) + \frac{\overline{\vec{\tau}_w}}{\rho h} - \frac{\overline{\vec{\tau}_b}}{\rho h} - \vec{f}k\times\vec{U} \tag{14}$$

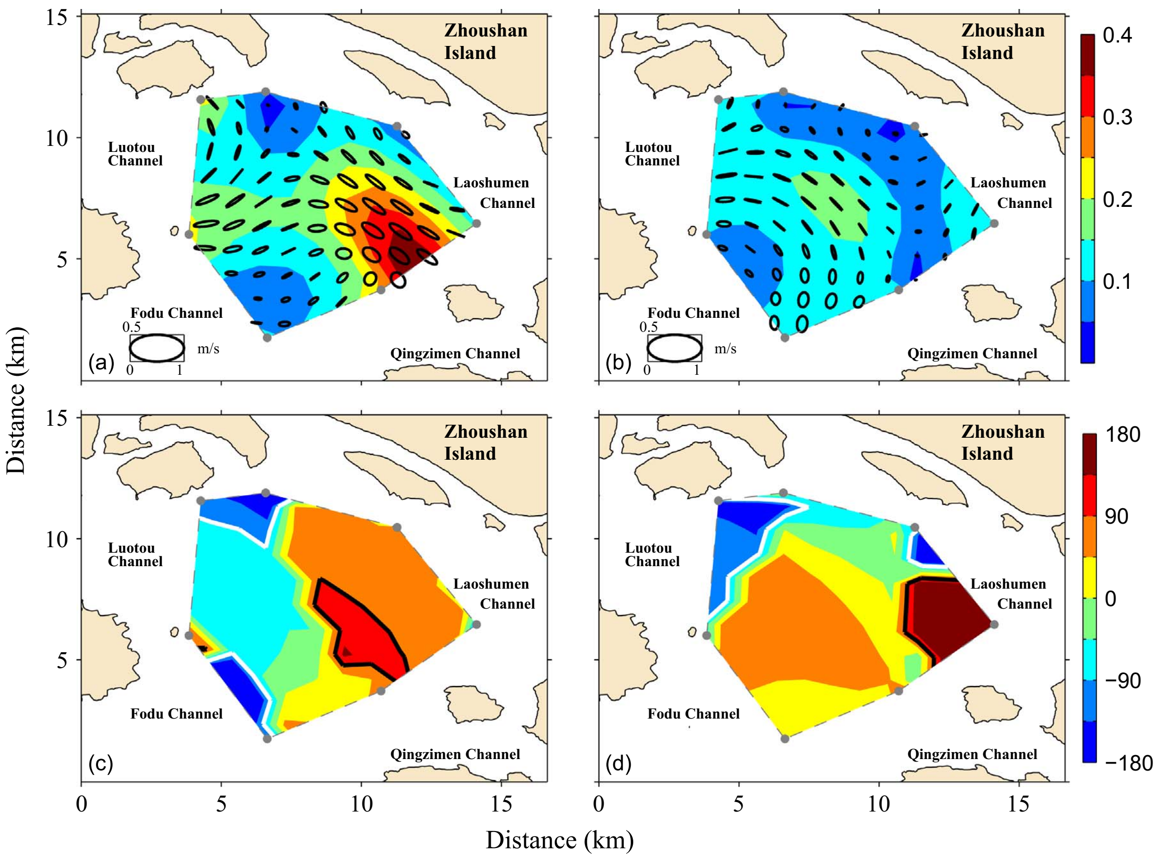

Fig. 7. The distribution of (a) the ratio of the velocity amplitudes of M_4 to M_2, (b) the ratio of the velocity amplitudes of M_6 to M_2, and the velocity phase in degrees of (c) $2M_2$-M_4, (d) $3M_2$-M_6. The black (white) lines in (c) and (d) indicate the 90° (−90°) contour lines.

Here, $\vec{i}, \vec{j}, \vec{k}$ are unit vectors in the eastward, northward, upward directions, respectively; $\nabla_h = \vec{i}\frac{\partial}{\partial x} + \vec{j}\frac{\partial}{\partial y}$; A_m is the horizontal eddy viscosity coefficient, which is set as 90 $m^2\,s^{-1}$ (Cáceres et al., 2003). Overbars denote a temporal average over one tidal cycle.

The term on the left-hand side of Eq. (14) is known as the tidally averaged advection of the tidal currents (Sheng and Wang, 2004). It is the forcing term for the residual flow and is part of the "tidal stress" (Nihoul and Ronday, 1975). It is balanced by the six terms on the right-hand side of Eq. (14). They are the pressure gradient of residual sea level ($-g\nabla_h\bar{\eta}$); advection of the residual currents ($\nabla_h(\vec{U}\vec{U})$); horizontal mixing of residual currents ($A_m\nabla_h\bullet(\nabla_h\vec{U})$); time mean wind stress ($\frac{\overline{\vec{\tau_w}}}{\rho h}$); time mean bottom stress ($\frac{\overline{\vec{\tau_b}}}{\rho h}$); Coriolis term ($-f\vec{k}\times\vec{U}$). The wind stress was calculated as $\vec{\tau_w} = C_w\rho_a|\vec{u_w}|\vec{u_w}$; here, $\vec{u_w} = u_w\vec{i} + v_w\vec{j}$, with u_w and v_w denoting the eastward and northward wind velocity components from reanalysis of data with six hour intervals (http://apps.ecmwf.int/datasets/data/interim-full-daily/); C_w denotes the wind-speed drag coefficient given by $C_w = 10^{-3}(0.63 + 0.066\sqrt{u_w^2 + v_w^2})$; $\rho_a = 1.29$ kg m^{-3} is air density (Smith and Banke, 1975). Here, we should note that, considering the spatial resolution of wind data (0.75°x0.75°), we use wind data from a single point (122.25°E, 30.0°N) to represent the whole observational region.

To quantify the role of each term in Eq. (14) in generating the residual current in ZTYB, the maximum and mean values of these terms are calculated during one M_2 tidal period (Table 3). The horizontal distributions of the six terms (except $-g\nabla_h\bar{\eta}$) in Eq. (14) are shown in Fig. 8a–f.

Fig. 8a shows that the tidally averaged advection term of the tidal currents ($|\nabla_h\bullet(\overline{\vec{u}'\vec{u}'})|$) is large where the residual current is strong, the maximum value being 3.36×10^{-4} m s^{-2} near Luotou channel. The mean value in the observation region is about 1.25×10^{-4} m s^{-2} (Table 3). The spatial distribution of the residual current advection term ($\nabla_h(\vec{U}\vec{U})$) (Fig. 8b) is similar to that of $|\nabla_h\cdot(\overline{\vec{u}'\vec{u}'})|$, with larger values near Luotou channel, and its value becomes about 2×10^{-5} m s^{-2} near Fodu channel. The maximum and mean values in the observation region are 1.76×10^{-4} m s^{-2} and 4.74×10^{-5} m s^{-2}, respectively. The mean value of $|\nabla_h(\vec{U}\vec{U})|$ takes up 37.9% of $|\nabla_h\cdot(\overline{\vec{u}'\vec{u}'})|$. The spatial distribution of the time mean horizontal mixing term ($A_m\nabla_h\bullet(\nabla_h\vec{U})$) (Fig. 8c) is different from that of the first two terms, and the mean value of $|A_m\nabla_h\bullet(\nabla_h\vec{U})|$ is only about 5×10^{-7} m s^{-2}, which takes up 0.4% of $|\nabla_h\bullet(\overline{\vec{u}'\vec{u}'})|$. The spatial pattern of the time mean bottom friction term ($\frac{\overline{\vec{\tau_b}}}{\rho h}$) (Fig. 8d) is similar to that of $|\nabla_h\bullet(\overline{\vec{u}'\vec{u}'})|$, with mean value about 8.1×10^{-6} m s^{-2}, which is about 6.5% of $|\nabla_h\bullet(\overline{\vec{u}'\vec{u}'})|$. The time mean wind stress term ($\left|\frac{\overline{\vec{\tau_w}}}{\rho h}\right|$) (Fig. 8f) is 5.18×10^{-6} m s^{-2}, which is 4.2% of $|\nabla_h\bullet(\overline{\vec{u}'\vec{u}'})|$. The mean value of the time mean Coriolis term ($-f\vec{k}\times\vec{U}$) (Fig. 8e) is 14.6% of $|\nabla_h\bullet(\overline{\vec{u}'\vec{u}'})|$ (Table 1). The CAT does not measure sea surface level in the observation region, therefore we can only estimate the time mean horizontal pressure gradient term ($-g\nabla_h\bar{\eta}$) by using Eq. (14). The results show that the mean value of $|g\nabla_h\bar{\eta}|$ in this region is

Table 3
Maximum and average values (in units of 10^{-6} m s^{-2}) of dynamic terms in the tidally averaged momentum equation, and percentages of each term relative to the forcing term.

	$\lvert\nabla_h\bullet(\overline{\vec{u}'\vec{u}'})\rvert$	$\lvert\nabla_h(\vec{U}\vec{U})\rvert$	$\lvert\nabla_h\bullet(A_m\nabla_h\vec{U})\rvert$	$\left\lvert\frac{\overline{\vec{\tau_b}}}{\rho h}\right\rvert$	$\lvert f\vec{k}\times\vec{U}\rvert$	$\left\lvert\frac{\overline{\vec{\tau_w}}}{\rho h}\right\rvert$
Maximum value	336	176	0.08	75	48.7	11.0
Percentage,%	100	52.4	0.02	22.3	14.5	3.3
Average value	125	47.4	0.5	8.1	18.3	5.2
Percentage,%	100	37.9	0.4	6.5	14.6	4.2

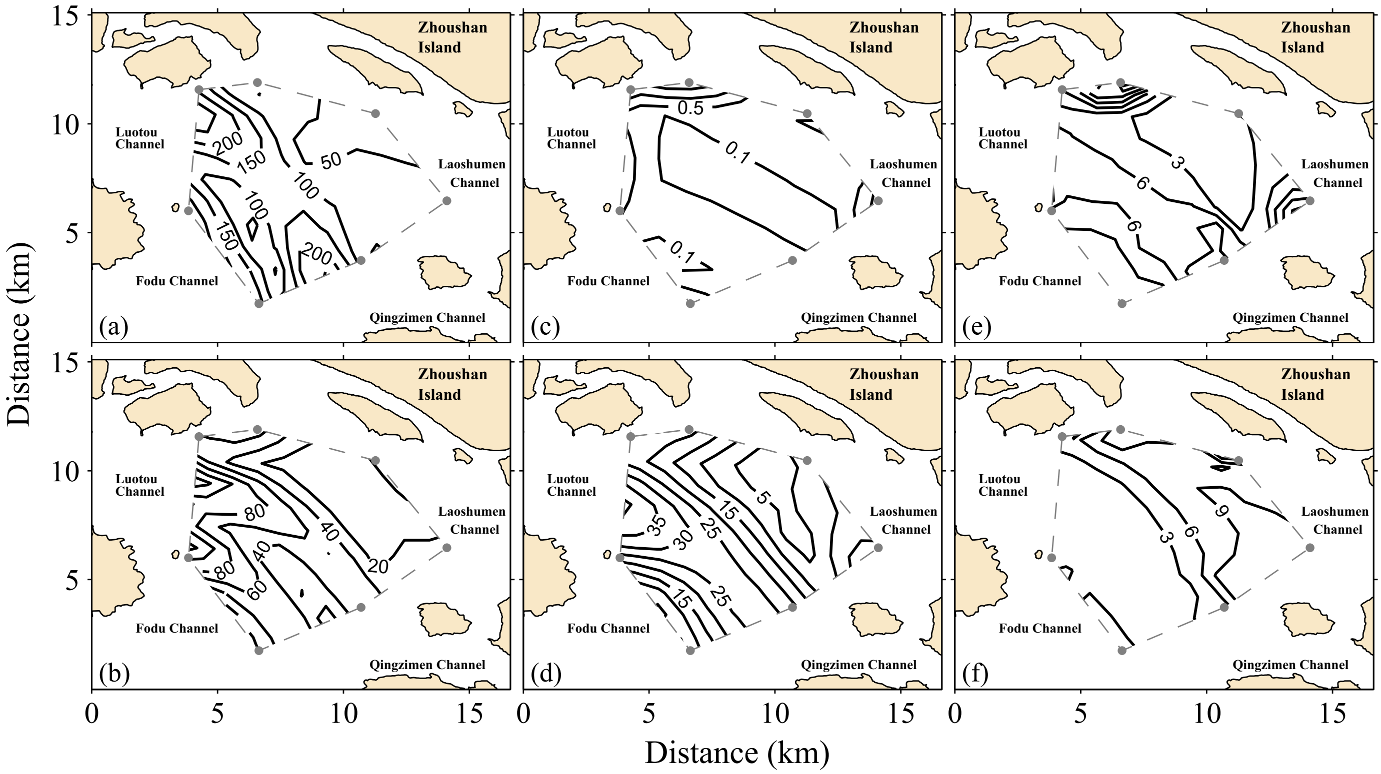

Fig. 8. Contour plot (in units of 10^{-6} m s^{-2}) for terms in Eq. (14): (a) $|\nabla_h \bullet (\overline{\vec{u}'\vec{u}'})|$, (b) $|\nabla_h(\vec{U}\vec{U})|$, (c) $|A_m \nabla_h \bullet (\nabla_h \vec{U})|$, (d) $\left|\frac{\vec{\tau}_b}{\rho h}\right|$, (e) $|f\vec{k} \times \vec{U}|$, (f) $\left|\frac{\vec{\tau}_w}{\rho h}\right|$.

about 4.55×10^{-5} m s^{-2}, which is about 36.4% of $|\nabla_h \bullet (\overline{\vec{u}'\vec{u}'})|$.

Therefore, the momentum equation (Eq. 14) of the residual currents in ZTYB is mainly balanced by the tidally averaged advection of the tidal currents, the averaged horizontal pressure gradient and the advection of the residual currents. In this region, wind stress, bottom friction and Coriolis force play relatively less important roles, and horizontal mixing is negligible.

5. Summary

In this study, we use observational data to reconstruct the horizontal distributions of M_4 and M_6 tidal ellipses and residual currents in ZTYB. Furthermore, we also discuss the dynamic mechanisms of the nonlinear tides and residual currents.

The mean semimajor and semiminor axis lengths of the M_4 current ellipses measured by CAT are 0.15 and 0.05 m s^{-1}, respectively. Also, substituting the measured tidal currents of the M_2 semidiurnal tidal constituent into the advection terms of the two-dimensional shallow-water equations we calculated the predicted M_4 (i.e., M_{4_cal}). The mean semimajor and semiminor axis lengths of the M_{4_cal} ellipses are 0.15 and 0.05 m s^{-1}, respectively. Comparing the velocity amplitudes of M_4 and M_{4_cal}, spatial points with good agreement mainly appear near the Luotou and Qinzimen channels, indicating that M_4 currents are mainly caused by the advection terms in the deep area, but are also generated by other factors in the observational regions where the values of the advection terms are small.

The mean semimajor and semiminor axis lengths of the M_6 current ellipses are 0.11 and 0.03 m s^{-1}. Substituting the M_2 tidal currents into the quadratic bottom friction terms of the two-dimensional shallow-water equations, we calculated the predicted M_6 (i.e., M_{6_cal}). The mean semimajor and semiminor axis lengths of the M_{6_cal} ellipses are 0.07 and 0.01 m s^{-1}, respectively, slightly smaller than the values for M_6. Comparing the velocity amplitudes of M_6 and M_{6_cal}, the tidal current ellipses of M_6 and M_{6_cal} are in good agreement in the area where depths are less than 20 m, indicating that the M_6 currents are mainly caused by the quadratic bottom friction terms in shallow waters, but the friction mechanisms have less impact in the deep area.

All these results indicate that the M_4 and M_6 tidal currents directly measured by the CAT are credible. To the best of our knowledge, this study is the first nonlinear tidal current measurement by CAT. Furthermore, we also demonstrate that the overtides M_4 and M_6 are mainly generated by the nonlinear advection and quadratic bottom friction terms of M_2, respectively.

Following previous studies (Sheng and Wang, 2004; Zhu et al., 2015) we also analyze the main dynamic processes responsible for the residual currents by using the averaged horizontal momentum equation. The predominant terms in balancing the momentum equation of the residual currents are advection of the tidal currents, horizontal pressure gradient, and advection of the residual currents, while the bottom friction and Coriolis force terms contribute less.

The analyses of M_4 and M_6 and the residual currents that we have carried out in this study are based on simultaneous current measurements by CAT. The results show the advantages of the CAT system for accurately mapping horizontal variations of tidal currents and residual currents. Our study suggests that CAT measurements have advantages for current monitoring over a large area and understanding dynamic mechanisms in coastal regions.

Acknowledgments

This study is supported by the National Natural Science Foundation of China (41276095, 41476020, 41576001, 41321004 and 41576031); the Scientific Research Fund of SIO under Grant JT1402; the projects of the State Key Laboratory of Satellite Ocean Environment Dynamics, SIO (SOEDZZ1501); the Open Fund of State Key Laboratory of Satellite Ocean Environment Dynamics, SIO (SOED1511), the National Programme on Global Change and Air-Sea Interaction (GASI-IPOVAI-01-02).

References

Aubrey, D.G., Speer, P.E., 1985. A study of nonlinear tidal propagation in shallow inlet/estuarine systems, Part I: observations. Estuar., Coast. Shelf Sci. 21, 185–205.

Blanton, J.O., Lin, G., Elston, S.A., 2002. Tidal current asymmetry in shallow estuaries and tidal creeks. Cont. Shelf Res. 22, 1731–1743.

Cáceres, M., Valle-Levinson, A., Atkinson, L., 2003. Observations of cross-channel structure of flow in an energetic tidal channel. J. Geophys. Res. 108 (C4), 3114. http://dx.doi.org/10.1029/2001JC000968.

Dong, L.X., Su, J.L., 1991a. Tide response and wave distortion in Xiangshan Bay, I, observation and analysis. Acta Ocean. Sin. 21 (2), 1–10, (in Chinese with English abstract).

Dong, L.X., Su, J.L., 1991b. Tide response and wave distortion in Xiangshan Bay, II, numerical modelling study in the Xiangshan Bay. Acta Ocean. Sin. 21 (1), 1–8, (in Chinese with English abstract).

Fang, G.H., 1987. Nonlinear effects of tidal friction. Acta Ocean. Sin. 6 (Supp I), S105–S122.

Friedrichs, G.T., Aubrey, D.G., 1988. Non-linear tidal distortion in shallow well-mixed estuaries: a synthesis. Estuar., Coast. Shelf Sci. 27, 521–545.

Godin, G., 1972. The Analysis of Tides. University of Toronto Press, Toronto.

Hansen, P.C., O'Leary, D.P., 1993. The use of the L-cure in the regularization of discrete ill-posed problems. SIAM J. Sci. Comput. 14 (6), 1487–1503.

Hench, J.L., Luettich, R.A., 2003. Transient tidal circulation and momentum balances at a shallow inlet. J. Phys. Oceanogr. 33, 913–932.

Hench, J.L., Blanton, B.O., Luettich, R.A., 2002. Lateral dynamic analysis and classification of barotropic tidal inlets. Cont. Shelf Res. 22, 2516–2631.

Le Provost, C., 1991. Generation of overtides and compound tides (review). In: Parker, B.B. (Ed.), Tidal Hydrodynamics. Wiley New York, USA, 269–295.

Nihoul, J.C.J., Ronday, F.C., 1975. The influence of the "tidal stress" on the residual circulation-application to the Southern Bight of the North Sea. Tellus 5, 484–489.

Park, J.-H., Kaneko, A., 2001. Computer simulation of the coastal acoustic tomography by a two-dimensional vortex model. J. Oceanogr. 57, 593–602.

Parker, B.B., 1991. The relative importance of the various nonlinear mechanisms in a wide range of tidal interactions (review). In: Parker, B.B. (Ed.), Tidal Hydrodynamics. Wiley New York, USA, 237–268.

Pawlowicz, R., Beardsley, B., Lentz, S., 2002. Classical tidal harmonic analysis including error estimates in MATLAB using T_TIDE. Comput. Geosci. 28, 929–937.

Pingree, R.D., Maddock, L., 1978. The M_4 tide in the english channel derived from a non-linear numerical model of the M_2 tide. Deep Sea Res. 25, 53–63.

Pingree, R.D., Maddock, L., 1980. Tidally induced residual flows around an island due to both frictional and rotational effects. J. Geophys. Res. 63, 533–546.

Sheng, J., Wang, L., 2004. Numerical study of tidal circulation and nonlinear dynamics in Lunenburg Bay, Nova Scotia. J. Geophys. Res. 109, C10018. http://dx.doi.org/10.1029/2004JC002404.

Smith, S.D., Banke, E.G., 1975. Variation of the sea surface drag coefficient with wind speed. Q. J. R. Meteorol. Soc. 101, 665–673.

Speer, P.E., Aubrey, D.G., 1985. A study of non-linear tidal propagation in shallow inlet/estuarine systems Part II: theory. Estuar., Coast. Shelf Sci. 21, 207–224.

Walters, R.A., Werner, F.E., 1991. Nonlinear generation of overtides compound tides, and residuals. In: Parker, B.B. (Ed.), Tidal Hydrodynamics. Wiley New York, USA, 269–295.

Yamaoka, H., Kaneko, A., Park, J.-H., Zheng, H., Gohda, N., Takano, T., Zhu, X.-H., Takasugi, Y., 2002. Coastal acoustic tomography system and its field application. IEEE J. Ocean. Eng. 27 (2), 283–295.

Zhu, X.-H., Kaneko, A., Wu, Q., Zhang, C., Taniguchi, N., Gohda, N., 2013. Mapping tidal current structures in Zhitouyang Bay, China, using coastal acoustic tomography. IEEE J. Ocean. Eng. 38 (2), 285–296.

Zhu, X.-H., Zhu, Z.-N., Guo, X., Ma, Y.-L., Fan, X., Dong, M., Zhang, C., 2015. Measurement of tidal and residual currents and volume transport through the Qiongzhou Strait using coastal acoustic tomography. Cont. Shelf Res. 108, 65–75.